Microstructural evolution induced by micro-cracking during fast lithiation of single-crystalline silicon

Yong Seok Choi [a,b], Matt Pharr [b], Chan Soon Kang [a], Seoung-Bum Son [a], Seul Cham Kim [a], Kee-Bum Kim [a,d], Hyunchul Roh [a], Se-Hee Lee [c], Kyu Hwan Oh [a], Joost J. Vlassak [b,*]

[a] Department of Materials Science and Engineering, Seoul National University, Seoul 151-742, Republic of Korea
[b] School of Engineering and Applied Sciences, Harvard University, Cambridge, MA 02138, USA
[c] Department of Mechanical Engineering, University of Colorado at Boulder, Boulder, CO 80309, USA
[d] High-Temperature Energy Materials Research Center, Korea Institute of Science and Technology, Seoul 136-791, Republic of Korea

HIGHLIGHTS

- Lithiation of Si results in various microstructures depending of crystal orientation.
- A complex vein-like microstructure of Li_xSi was observed in {100} oriented Si.
- Micro-cracks provide a fast path for Li diffusion and cause a non-uniform lithiation.
- Crystalline Li_xSi plays an important role in micro-crack generation.

ARTICLE INFO

ABSTRACT

We report observations of microstructural changes in {100} and {110} oriented silicon wafers during initial lithiation under relatively high current densities. Evolution of the microstructure during lithiation was found to depend on the crystallographic orientation of the silicon wafers. In {110} silicon wafers, the phase boundary between silicon and Li_xSi remained flat and parallel to the surface. In contrast, lithiation of the {100} oriented substrate resulted in a complex vein-like microstructure of Li_xSi in a crystalline silicon matrix. A simple calculation demonstrates that the formation of such structures is energetically unfavorable in the absence of defects due to the large hydrostatic stresses that develop. However, TEM observations revealed micro-cracks in the {100} silicon wafer, which can create fast diffusion paths for lithium and contribute to the formation of a complex vein-like Li_xSi network. This defect-induced microstructure can significantly affect the subsequent delithiation and following cycles, resulting in degradation of the electrode.

1. Introduction

Because of their high power densities, lithium-ion batteries are employed in applications that are especially sensitive to weight and size, such as portable electronic devices and electric vehicles [1–6]. Generally, graphite-based materials are used for anodes due to their low cost and stable performance, but they have a limited capacity of 372 mAh g^{-1} [7]. Silicon has drawn considerable attention as one of the most promising anode materials due to its huge theoretical capacity of ~4200 mAh g^{-1} ($Li_{22}Si_5$) [8–11]. Associated with this large capacity, insertion of lithium into silicon causes large

volumetric expansion in the range of 300%–400% [11–14]. Under constraint, this expansion can generate stresses, leading to fracture and pulverization of the electrode, degrading the capacity of the electrode during cycling. To prevent this mechanical degradation, nanostructures such as nanowires, thin films, hollow nanoparticles, 3D porous nanoparticles, and Si–C composites are being investigated [15–26].

Although silicon transforms to several distinct silicon–lithium crystalline phases at elevated temperature [10], it is well known that electrochemical lithiation of silicon at room temperature results in an amorphous phase of lithiated silicon [5,12,27–29]. Obrovac et al. [5] suggested that the lithiation of crystalline silicon is a two-phase reaction in which a reaction front separates the growing amorphous lithiated phase from pristine crystalline silicon. Chon et al. [30] showed clear images of a crystalline-to-

amorphous phase transformation that occurs during initial lithiation of a {100} silicon wafer. Furthermore, Lee et al. [31] demonstrated anisotropic deformation of silicon nanopillars during lithiation. A number of first-principles calculations and experimental studies have shown that the lithiation reaction is anisotropic and fastest in the <110> direction [31–34]. If lithiation is controlled by this reaction mechanism as opposed to diffusion through the lithiated phase, anisotropic expansion may occur [34,35]. Most previous studies have assumed that lithium insertion and reaction processes at the reaction front are spatially uniform. However, defects, geometrical instabilities, and solid-electrolyte interface (SEI) layers can cause spatially inhomogeneous lithiation. These inhomogeneities may lead to a non-uniform strain distribution in the lithiated phase, resulting in fracture and the degradation of the capacity of the battery. In addition, fast transport of both electrons and lithium ions is desired for achieving a high charging/discharging rate in lithium-ion batteries. Several researchers have already reported a number of microstructural observations of silicon wafers during lithiation at lower current densities [30,34]. However, little is known concerning the microstructural evolution during lithiation at elevated current densities.

In this paper, we report on an experimental study in which we applied relatively large lithiation current densities to {100} and {110} oriented silicon wafers to evaluate the effect of crystal orientation on the microstructural evolution of the lithiated phase. We observe uniform lithiation of {110} silicon wafers, but a complex microstructure with micro-cracks in {100} silicon wafers. Since these micro-cracks only occur in the {100} substrates, we suggest that the formation of crystalline Li_xSi depends on crystal orientation and plays an important role in micro-crack generation. These observations have important ramifications for mitigation of damage during lithiation of crystalline silicon.

2. Experimental procedures

Single-side polished silicon wafers of two orientations, {100} and {110}, were used as working electrodes. The wafers were not etched prior to use. All wafers were 500 μm thick, were doped with boron, and had a resistivity of 1–30 Ω cm. The wafers were cut into 5 mm × 5 mm sections, cleaned with methanol and acetone, and assembled into electrochemical cells using standard 2032 half coin cells with lithium foil as the counter electrode. Copper foil was used as a current collector. The electrolyte was a 1 M solution of $LiPF_6$ in 1:1 (vol%) ethylene carbonate (EC):diethyl carbonate (DEC). Once assembled, the silicon electrodes were lithiated at a constant current density of 500 μA cm^{-2} for different amounts of time. Three sets of samples were lithiated under identical conditions to confirm the microstructural observations. After lithiation, the electrodes were removed from the half coin cell, rinsed in dimethyl carbonate (DMC), and dried for 10 min. To prevent reactions with ambient air, all processes including assembly and disassembly of the cells were performed inside a glovebox filled with high-purity argon. Similar experiments were also performed using a custom-fabricated hermetic Teflon cell to alleviate any concerns about the spring in the coin cell adversely affecting the results in any way. We observed microstructural evolution in {100} and {110} wafers similar to those observed in the coin cells, indicating a negligible effect of the spring-induced pressure on our results (results not shown).

The microstructure of the lithiated phase was observed inside a focused ion beam (FIB, FEI NOVA200 DualBeam) system equipped with an air-lock chamber. Samples were cross-sectioned using a beam of Ga ions and then observed using scanning electron microscopy (SEM). Platinum was deposited for surface protection. After imaging, sample cross-sections were lifted out and attached to Cu TEM grids using a manipulating probe. A high-resolution transmission electron microscope (HR-TEM, Technai F20) operating at 200 keV was used for detailed analysis of the microstructure of the lithiated phase. Selected area electron diffraction (SAED) patterns and Fourier transforms were analyzed using a software package (Gatan, Digital Micrograph). For phase determination, X-ray diffraction data was collected with an X-ray diffractometer (XRD, Bruker, D8 Advance) using Cu-K$_\alpha$ radiation. To prevent air exposure during sample transfer, all samples were transported inside an argon-filled portable chamber with an air-lock.

3. Results and discussion

Fig. 1 shows SEM images of {100} and {110} silicon wafers after initial lithiation under constant current densities of 500 μA cm^{-2} for 2.5 h. The surface morphology and the microstructure of the lithiated phase clearly depend on the orientation of the silicon. Fig. 1a shows a typical SEM image of the surface of a {110} silicon substrate. Evidently all regions maintain a relatively clean surface, and surface cracks are not observed. As shown in Fig. 2b, a planar phase boundary between the Li_xSi layer and the crystalline silicon is observed. The total thickness of the Li_xSi layer is approximately 2.39 μm (dashed red (in the web version) line in Fig. 2b). It should be noted that the average measured thickness of the Li_xSi layer is significantly smaller than the calculated value (4.8 μm) based on the total applied current density [30]. Since we applied a high current density of 500 μA cm^{-2}, a large overpotential results. Thus, a large amount of lithium is consumed in side reactions, such as SEI formation [36,37].

In {100} silicon wafers, however, some regions maintain a pristine surface similar to the {110} silicon wafer (Fig. 1c), while others are riddled with surface cracks (Fig. 1e). Similar surface features were also observed on samples lithiated for 1 h, but fewer regions with surface cracks were observed as compared to the 2.5 h lithiated sample. The lengths of the surface cracks were typically several tens of micrometers. If the lithiation reaction front remains flat, cracking is not expected during lithiation of crystalline Si wafer because the lithiated phase will develop a compressive biaxial stress state [35]. In contrast, the observation of surface cracks in {100} silicon wafers (Fig. 1e) indicates a different physical picture, namely a non-planar reaction front, which can lead to a more complicated state of stress and thereby generate surface cracks. Fig. 1f shows a cross-sectional image of a region where surface cracks occur in the {100} silicon wafer. The image reveals a microstructure that contains a complex vein-like network of Li_xSi layers in a crystalline silicon matrix. The Li_xSi layers are several hundreds of nanometers in width and penetrate more than 6 μm into the silicon wafer. The Li_xSi layers in the network seem to follow a preferred direction inclined relative to the surface of the substrate. In contrast, as shown in Fig. 1d, a planar phase boundary between the Li_xSi layer and the crystalline silicon is observed in regions away from surface cracks. This morphology is similar to that of the {110} silicon wafers, and the average thickness of the Li_xSi layer is approximately 1.42 μm (dashed red (in the web version) lines in Fig. 1d).

To provide insight into the development of the microstructure, samples from regions with surface cracks were removed from a {100} silicon wafer and observed using HR-TEM. Fig. 2a shows cross-sectional TEM images of the wafer after one hour of lithiation at 500 μA cm^{-2}. The white arrow points from the surface of the silicon wafer toward the interior. The image shows a relatively simple network of Li_xSi that displays two preferred directions: one almost parallel to the surface of the wafer and the other at an angle of approximately 45–55° to the surface. The width of each Li_xSi layer is approximately tens of nanometers, and the layers penetrate approximately 3 μm into the silicon. Fig. 2c shows the

{110} silicon wafer	{100} silicon wafer	
No surface cracks	**Away from surface cracks**	**Near surface cracks**
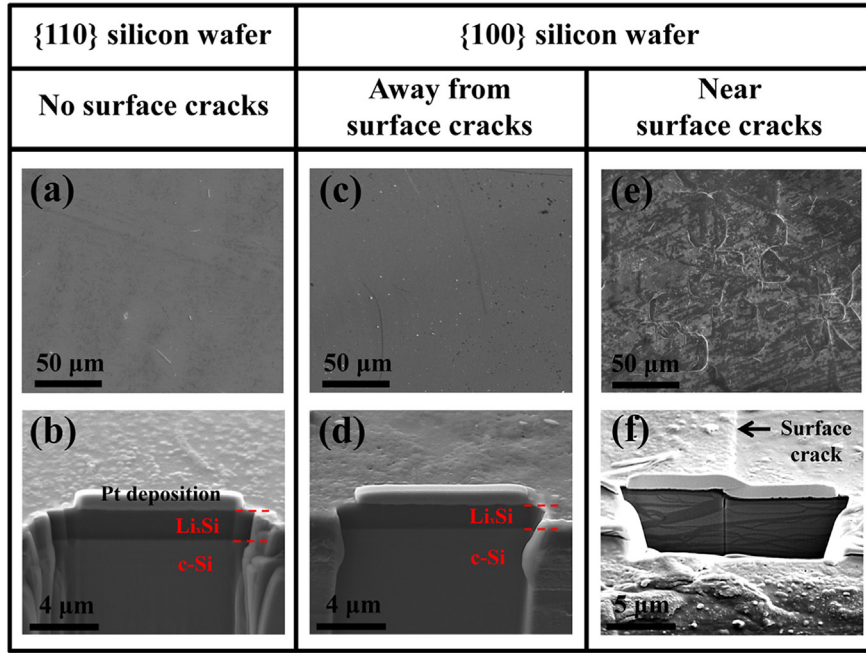
Fig. 1. SEM images of silicon wafers that were lithiated at 500 μA cm^{-2} for 2.5 h. (a) Surface and (b) cross-sectional images of the {110} silicon wafer showing no surface cracks. (c) Surface and (d) cross-sectional images of the {100} silicon wafer away from the surface cracks, and (e) surface and (f) cross-sectional images of an area where surface cracks occur.

microstructure after 2.5 h of lithiation. The width of the individual Li$_x$Si layers is now several hundreds of nanometers, and multiple channels interconnecting the Li$_x$Si layers have been created, although they still show the same preferred orientation. The high-resolution images and the Fourier transforms of the regions (Fig. 2b and d) provide phase information: the thin layers consist of amorphous Li$_x$Si and are separated by single-crystalline silicon. The high-resolution images indicate that the boundary between both phases is very sharp with a width of only a few nanometers. We consider two other possible mechanisms for creating such a microstructure: an instability of the reaction front due to aniso-tropic reaction kinetics or formation of defects that provide fast paths for lithium diffusion.

Fig. 2. TEM images of a lithiated {100} silicon wafer subjected to a current density of 500 μA cm^{-2}. (a) Bright field image of the silicon wafer lithiated for 1 h. (b) High-resolution image and corresponding Fourier transform image of the region indicated in (a). (c) Bright field image of the silicon wafer lithiated for 2.5 h. (d) High-resolution image and corresponding Fourier transform image of the region indicated in (c).

Anisotropic reaction kinetics in crystalline silicon have been observed in a number of studies [31,34,38]. It is possible that these kinetics can result in an instability such as non-planar growth along the direction with the fastest reaction rate. To examine this possi-bility, we now evaluate the driving force for the movement of the reaction front, as discussed in detail in a previous paper [35]. The reaction at the interface can be represented by

$$\text{Li} + \frac{1}{x}\text{Si} = \frac{1}{x}\text{Li}_x\text{Si}. \tag{1}$$

Associated with this reaction is a net change in free energy, ΔG, given by [35]

$$\Delta G = \Delta G_r - e\Phi + \frac{1}{x}\left(\sigma_h^{Si}\Omega^{Si} - \sigma_h^{Li_xSi}\Omega^{Li_xSi}\right), \tag{2}$$

where e is the elementary charge, Φ is the applied voltage, α_h is the hydrostatic stress, Ω is the atomic volume, and ΔG_r is the change in free energy associated with the lithiation reaction when the applied voltage and the stress in both phases vanish. We have neglected any dissipation at the electrolyte/electrode interfaces, inside the elec-trodes, and in the electrolyte. In our sign convention, a positive value of Φ promotes lithiation of silicon, and a more negative value of ΔG represents a larger driving force for the reaction. A compressive hydrostatic stress in the pure silicon phase promotes lithiation while a compressive stress in the lithiated silicon retards it.

The net change in free energy is the driving force for the movement of the reaction front. The velocity of the reaction front will increase as the magnitude of the driving force increases. We take the reaction to be thermally activated, and, as an example, described by a familiar kinetic model [39]:

$$V = V_0 \exp\left(-\frac{Q}{kT}\right)\left[\exp\left(-\frac{\Delta G}{kT}\right) - 1\right], \tag{3}$$

where V_0 is a parameter analogous to the exchange current density, Q the activation energy, k the Boltzmann constant, and T the

absolute temperature. The prefactor $V_0 \exp(-Q/kT)$ may be a function of the crystallographic orientation, as discussed elsewhere [34].

To illustrate the effects of the stress on the reaction, we will consider accommodation of lithium via two simple mechanisms: growth of a planar reaction front and growth of a small perturbation that eventually leads to a vein-like Li_xSi network, as illustrated in Fig. 3. These two cases represent the different structures observed in the experiments. For the growth of a flat reaction front (Fig. 3a), the lithiated silicon phase is under equal biaxial compression equal to the yield strength, $\sigma_Y^{Li_xSi}$, and the hydrostatic stress in the lithiated phase is $\sigma_h^{Li_xSi} = -2\sigma_Y^{Li_xSi}/3$. The stress in the crystalline silicon phase is zero everywhere, $\sigma_h^{Si} = 0$. Using a value of $\sigma_Y^{Li_{3.75}Si} = 500$ MPa [40], we obtain $\sigma_h^{Li_xSi} = -0.33$ GPa. Using $\Omega^{Li_xSi} = 7.6 \times 10^{-29}$ m^3 and $x = 3.75$ [34], the contribution of the stress to the free energy, $1/x(\sigma_h^{Si}\Omega^{Si} - \sigma_h^{Li_xSi}\Omega^{Li_xSi})$, is 0.042 eV for growth of the planar reaction front.

Consider now a very small perturbation in the reaction front (Fig. 3b). Because the reaction front is no longer planar, a stress state develops in both the lithiated silicon and in the single-crystalline silicon. To first order, the stress state in the vicinity of the perturbation can be approximated by the stress field around a misfitting sphere. From elasticity, one obtains [41]

$$\sigma_r^{Li_xSi} = \sigma_\theta^{Li_xSi} = -p, \quad \sigma_r^{Si} = -p\frac{a^3}{r^3}, \quad \sigma_\theta^{Si} = \frac{p}{2}\frac{a^3}{r^3}$$

$$p = \frac{2E^{Li_xSi}E^{Si}\varepsilon_{mf}}{2E^{Si}(1 - 2\nu^{Li_xSi}) + E^{Li_xSi}(1 + \nu^{Si})}, \tag{4}$$

where a is the radius of the sphere, r is the radial position from the center of the sphere, E represents the elastic modulus, ν represents Poisson's ratio, and ε_{mf} represents the mismatch in linear strain. Near the interface, $r = a$, the hydrostatic stresses, $\sigma_h = (\sigma_r + 2\sigma_\theta)/3$, are $\sigma_h^{Li_xSi} = -p$ and $\sigma_h^{Si} = 0$. Using representative values of $E^{Si} = 160$ GPa [42], $E^{Li_xSi} = 12$ GPa [43], $\nu^{Si} = 0.22$ [42], $\nu^{Li_xSi} = 0.26$ [42], $\varepsilon_{mf} = 0.55$ (for a 280% increase in volume upon full lithiation), we find $\sigma_h^{Li_xSi} = -11$ GPa. Thus, the contribution of the stress to the free energy, $1/x(\sigma_h^{Si}\Omega^{Si} - \sigma_h^{Li_xSi}\Omega^{Li_xSi})$, is estimated at 1.38 eV for

growth of a (spherical) perturbation. We should point out that the solution from elasticity is not exact because of large deformation effects and plastic deformation. However, we have performed a full elastic−plastic and large deformation simulation in ABAQUS for a spherical particle of lithiated silicon in a pure silicon matrix. These results give a contribution of the stress to the free energy of 0.92 eV.

This analysis shows that the stress has a relatively large retarding effect for growth of a perturbation and a relatively small retarding effect for growth of a planar reaction front. In fact, within the context of the presented kinetic model (Equations (2)–(3)), no value of applied voltage will result in preferential growth of a perturbation. This assertion persists even considering the variation in the measured values of the reaction rates along different crystallographic orientations, (i.e. $V_0 \exp(-Q/kT)$ is a function of orientation) as measured by Pharr et al. [34]. For instance, since the rate of reaction (neglecting stress effects), V_0, is faster along <110> than along <100>, it seems possible that for a {100} wafer, lithiation may occur via a perturbation along the <110> direction. However, the energy penalty associated with the stresses generated in forming such a perturbation outweighs the gain in the reaction rate along the <110> direction. Thus, within the context of this model, the lithiated phase will always grow by motion of a flat reaction front for silicon wafers of any orientation.

The above calculation suggests that the stress has a very large stabilizing effect − i.e, a complex geometry of Li_xSi layers cannot form by a perturbation of the reaction front. Instead, we propose that defects provide a fast path for lithium diffusion, thereby leading to non-uniform lithiation. Fig. 4 shows TEM images of the region delineated by the green square in Fig. 2a. Line structures with a width of a few nanometers can be seen in Fig. 4, which lie along the same preferred directions as the Li_xSi network shown in Fig. 2a. We believe that these line structures are micro-cracks that provide fast diffusion paths for lithium. The HR-TEM image shows the region of the tip of the micro-crack as indicated by the varying contrast. Moreover, the Fourier transform image shown in Fig. 4 indicates that the line structures lie along the {111} planes: the preferential cleavage planes in silicon. Since the cross-section was made parallel to a [110] direction in the surface of the wafer, the observed micro-cracks both parallel to the surface and at an angle of ∼54° to the surface may indicate cracking between {111} plane. Once several micro-cracks form, the local stress field near the crack becomes more complex and a network of interconnecting cracks can develop.

Fig. 5 shows XRD patterns for the {100} and {110} silicon substrates before and after lithiation. The broad peak around 18° is attributed to the borosilicate glass capillary tube of the specimen holder. Before lithiation, the {100} and the {110} silicon electrodes only display silicon peaks. After 2.5 h of lithiation, the XRD pattern for the {100} wafer clearly shows the formation of a crystalline phase, $Li_{15}Si_4$. This finding agrees with the observation in a number of studies that highly lithiated amorphous silicon anodes can crystallize below 50 mV to form the $Li_{15}Si_4$ phase [5,10,12,27,44]. However, this result conflicts with our TEM study discussed previously in Fig. 2, in which only an amorphous Li_xSi phase was observed. Thus, we believe that the $Li_{15}Si_4$ phase is amorphized during the TEM sample preparation process as a result of gallium ion bombardment [29,45]. In contrast, the XRD pattern for the {110} silicon wafer shows a very weak peak at 23° suggesting the presence of a very small amount of crystalline $Li_{15}Si_4$, and broad peak around 43°. According to Obrovac et al. [5], this broad peak is caused by the amorphous Li_xSi phase.

In general, multiple kinetic processes can significantly contribute during the first lithiation [34,46]. If we compare the XRD data obtained before and after lithiation, broad peaks for amorphous Li_xSi phase can be seen around 22°−28° and 38°−45° in both
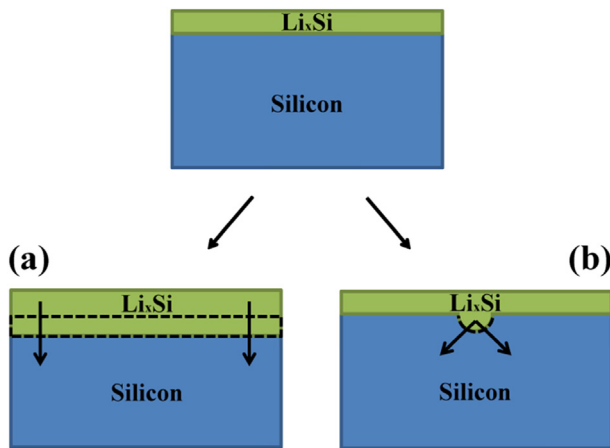

Fig. 3. The schematic shows a configuration of a lithiated silicon film on a crystalline silicon substrate. The dashed regions represent growth from the initial configuration. (a) The bottom left schematic illustrates lithium insertion by (continued) growth of a flat reaction front, (b) while the bottom right schematic illustrates lithium insertion by growth of a perturbation.
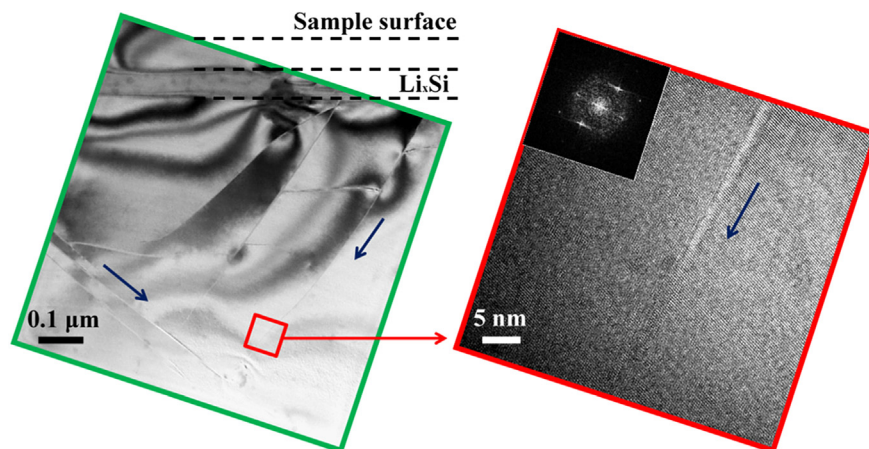
Fig. 4. TEM images of a lithiated {100} silicon wafer under a current density of 500 μA cm^{-2} for 1 h (green square in Fig. 2a). The blue arrows indicate the <111> direction. The line structures are micro-cracks that act as fast diffusion paths for lithium. (For interpretation of the references to color in this figure legend, the reader is referred to the web version of this article.)
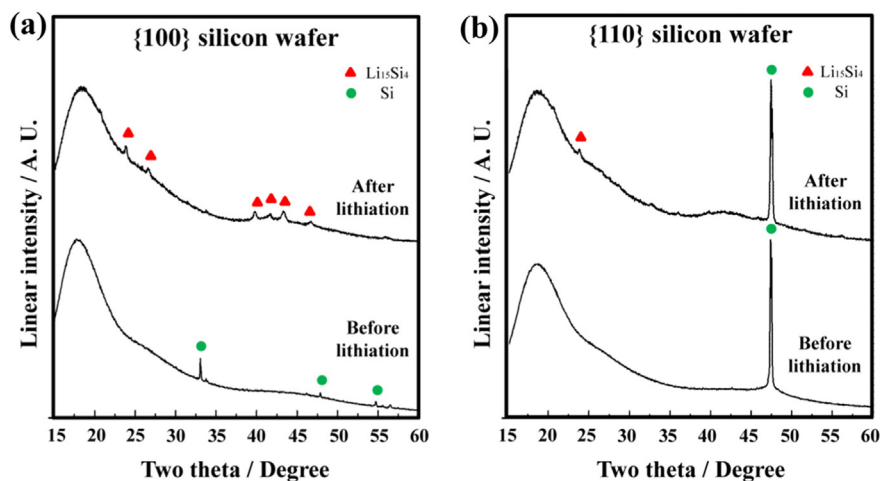
Fig. 5. XRD patterns of (a) {100} and (b) {110} silicon wafer before and after lithiation under a current density of 500 μA cm^{-2} for 2.5 h.

{100} and {110} silicon wafer. However, the crystalline $Li_{15}Si_4$ phase in the {100} silicon wafers seems more prevalent. Consequently, we believe that crystallization of the lithiated silicon in the {100} electrode contributes to the generation of micro-cracks. Gu et al. [47] reported that crystallization of $Li_{15}Si_4$ from amorphous Li_xSi is a congruent process in which the chemical composition remains constant. As such, the transformation does not require long-range diffusion but instead a simple local atomic rearrangement, and it is expected that the volume change during crystallization is small compared to that of lithiation. However, during lithiation, the lithiated silicon flows plastically due to the extreme volume expansion [48]. Thus, even a very small contraction during crystallization can result in local tensile stresses, thereby generating cracks. Therefore, we believe crystallization of the lithiated silicon results in micro-cracking in the {100} silicon wafers. The complex vein-like microstructures induced by micro-cracking significantly affects the subsequent delithiation and the following charge/discharge cycles.

4. Conclusion

We have studied the microstructural evolution of both {100} and {110} silicon wafers during initial lithiation under relatively high current densities. We observed surface cracks and a complex vein-like network of Li_xSi layers in {100} silicon wafers during initial lithiation, whereas no such structures were seen in {110} silicon wafers. A calculation reveals that these structures are energetically unfavorable due to the large hydrostatic stresses associated with them. Instead, we propose that the formation of micro-cracks in {100} wafers leads to fast diffusion paths for lithium. We further suggest that the formation of crystalline $Li_{15}Si_4$ in {100} silicon wafers may lead to localized tensile stresses, thereby generating these micro-cracks. Our observations provide insight into the mechanisms governing non-uniform lithiation and cracking of crystalline silicon, which should be avoided to prevent degradation of the electrode.

References

[1] R. Marom, S.F. Amalraj, N. Leifer, D. Jacob, D. Aurbach, J. Mater. Chem. 21 (2011) 9938–9954.
[2] B.L. Ellis, K.T. Lee, L.F. Nazar, Chem. Mater. 22 (2010) 691–714.
[3] S.D. Beattie, D. Larcher, M. Morcrette, B. Simon, J.-M. Tarascon, J. Electrochem. Soc. 155 (2008) A158–A163.
[4] J.-M. Tarascon, M. Armand, Nature 414 (2001) 359–367.
[5] M.N. Obrovac, L. Christensen, Electrochem. Solid-State Lett. 7 (2004) A93–A96.
[6] M. Armand, J.-M. Tarascon, Nature 451 (2008) 652–657.
[7] J.R. Dahn, T. Zheng, Y. Liu, J.S. Xue, Science 270 (1995) 590–593.
[8] W.-J. Zhang, J. Power Sources 196 (2011) 13–24.
[9] B.A. Boukamp, G.C. Lesh, R.A. Huggins, J. Electrochem. Soc. 128 (1981) 725–729.
[10] Y. Wang, J. Dahn, J. Electrochem. Soc. 153 (2006) A2314–A2318.
[11] U. Kasavajjula, C. Wang, A.J. Appleby, J. Power Sources 163 (2007) 1003–1039.
[12] M.N. Obrovac, L.J. Krause, J. Electrochem. Soc. 154 (2007) A103–A108.
[13] L.Y. Beaulieu, K.W. Eberman, R.L. Turner, L.J. Krause, J.R. Dahn, Electrochem. Solid-State Lett. 4 (2001) A137–A140.
[14] S. Golmon, K. Maute, S.-H. Lee, M.L. Dunn, Appl. Phys. Lett. 97 (2010) 033111.
[15] H. Wu, G. Chan, J.W. Choi, I. Ryu, Y. Yao, M.T. McDowell, S.W. Lee, A. Jackson, Y. Yang, L. Hu, Y. Cui, Nat. Nanotechnol. 7 (2012) 310–315.
[16] C.K. Chan, H. Peng, G. Liu, K. McIlwrath, X.F. Zhang, R.A. Huggins, Y. Cui, Nat. Nanotechnol. 3 (2008) 31–35.
[17] Q. Zhang, W. Zhang, W. Wan, Y. Cui, E. Wang, Nano Lett. 10 (2010) 3243–3249.
[18] T. Takamura, S. Ohara, M. Uehara, J. Suzuki, K. Sekine, J. Power Sources 129 (2004) 96–100.
[19] S.K. Soni, B.W. Sheldon, X. Xiao, A. Tokranov, Scr. Mater. 64 (2011) 307–310.
[20] J. Cho, J. Mater. Chem. 20 (2010) 4009–4014.
[21] T. Song, J. Xia, J.-H. Lee, D.H. Lee, M.-S. Kwon, J.-M. Choi, J. Wu, S.K. Doo, H. Chang, W.I. Park, D.S. Zang, H. Kim, Y. Huang, K.-C. Hwang, J.A. Rogers, U. Paik, Nano Lett. 10 (2010) 1710–1716.
[22] R. Yi, F. Dai, M.L. Gordin, H. Sohn, D. Wang, Adv. Energy Mater. 3 (2013) 1507–1515.
[23] R. Yi, J. Zai, F. Dai, M.L. Gordin, D. Wang, Electrochem. Commun. 36 (2013) 29–32.
[24] C.-H. Yim, F.M. Courtel, Y. Abu-Lebdeh, J. Mater. Chem. A 1 (2013) 8234–8243.
[25] J. Niu, J.Y. Lee, Electrochem. Solid-State Lett. 5 (2002) A107–A110.
[26] P.-C. Chen, J. Xu, H. Chen, C. Zhou, Nano Res. 4 (2011) 290–296.
[27] J. Li, J.R. Dahn, J. Electrochem. Soc. 154 (2007) A156–A161.
[28] K. Zhao, W.L. Wang, J. Gregoire, M. Pharr, Z. Suo, J.J. Vlassak, E. Kaxiras, Nano Lett. 11 (2011) 2962–2967.
[29] S.-B. Son, J.E. Trevey, H. Roh, S.-H. Kim, K.-B. Kim, J.S. Cho, J.-T. Moon, C.M. DeLuca, K.K. Maute, M.L. Dunn, H.N. Han, K.H. Oh, S.-H. Lee, Adv. Energy Mater. 1 (2011) 1199–1204.
[30] M.J. Chon, V.A. Sethuraman, A. McCormick, V. Srinivasan, P.R. Guduru, Phys. Rev. Lett. 107 (2011) 045503.
[31] S.W. Lee, M.T. McDowell, J.W. Choi, Y. Cui, Nano Lett. 11 (2011) 3034–3039.
[32] J.L. Goldman, B.R. Long, A.A. Gewirth, R.G. Nuzzo, Adv. Funct. Mater. 21 (2011) 2412–2422.
[33] X.H. Liu, J.W. Wang, S. Huang, F. Fan, X. Huang, Y. Liu, S. Krylyuk, J. Yoo, S.A. Dayeh, A.V. Davydov, S.X. Mao, S.T. Picraux, S. Zhang, J. Li, T. Zhu, J.Y. Huang, Nat. Nanotechnol. 7 (2012) 749–756.
[34] M. Pharr, K. Zhao, X. Wang, Z. Suo, J.J. Vlassak, Nano Lett. 12 (2012) 5039–5047.
[35] K. Zhao, M. Pharr, Q. Wan, W.L. Wang, E. Kaxiras, J.J. Vlassak, Z. Suo, J. Electrochem. Soc. 159 (2012) A238–A243.
[36] C.K. Chan, R. Ruffo, S.S. Hong, Y. Cui, J. Power Sources 189 (2009) 1132–1140.
[37] M.B. Pinson, M.Z. Bazant, J. Electrochem. Soc. 160 (2013) A243–A250.
[38] S.W. Lee, M.T. McDowell, L.A. Berla, W.D. Nix, Y. Cui, Proc. Natl. Acad. Sci. 109 (2012) 4080–4085.
[39] J.O. Bockris, A.K. Reddy, Modern Electrochemistry 2B: Electrodics in Chemistry, Engineering, Biology and Environmental Science, Springer, 2001.
[40] M. Pharr, Z. Suo, J.J. Vlassak, Nano Lett. 13 (2013) 5570–5577.
[41] J. Selsing, J. Am. Ceram. Soc. 44 (1961) 419.
[42] L.B. Freund, S. Suresh, Thin Film Materials: Stress, Defect Formation and Surface Evolution, Cambridge University Press, UK, 2004.
[43] B. Hertzberg, J. Benson, G. Yushin, Electrochem. Commun. 13 (2011) 818–821.
[44] X.H. Liu, H. Zheng, L. Zhong, S. Huang, K. Karki, L.Q. Zhang, Y. Liu, A. Kushima, W.T. Liang, J.W. Wang, J.-H. Cho, E. Epstein, S.A. Dayeh, S.T. Picraux, T. Zhu, J. Li, J.P. Sullivan, J. Cumings, C. Wang, S.X. Mao, Z.Z. Ye, S. Zhang, J.Y. Huang, Nano Lett. 11 (2011) 3312–3318.
[45] V.L. Chevrier, J.W. Zwanziger, J.R. Dahn, J. Alloys Compd. 496 (2010) 25–36.
[46] E.D. Cubuk, W.L. Wang, K. Zhao, J.J. Vlassak, Z. Suo, E. Kaxiras, Nano Lett. 13 (2013) 2011–2015.
[47] M. Gu, Z. Wang, J.G. Connell, D.E. Perea, L.J. Lauhon, F. Gao, C. Wang, ACS Nano 7 (2013) 6303–6309.
[48] V.A. Sethuraman, M.J. Chon, M. Shimshak, V. Srinivasan, P.R. Guduru, J. Power Sources 195 (2010) 5062–5066.